




Spectral modulation of high-order harmonics in relativistic laser-solid interactionB. Y. Li ^{1,2} F. Liu,^{1,2,*} M. Chen ^{1,2} X. H. Yuan,^{1,2} Z. M. Sheng ^{1,2,3} and J. Zhang^{1,2,3}¹Key Laboratory for Laser Plasmas (Ministry of Education), School of Physics and Astronomy, Shanghai Jiao Tong University, Shanghai 200240, China²Collaborative Innovation Center of IFSA (CICIFSA), Shanghai Jiao Tong University, Shanghai 200240, China³Tsung-Dao Lee Institute, Shanghai Jiao Tong University, Shanghai 200240, China

(Received 8 May 2023; accepted 5 February 2024; published 26 February 2024)

Spectral modulation of high-order harmonics generated in relativistic laser-solid interaction is investigated. Numerical simulations show that the modulation depends on surface plasma density profile, resulting in spectral envelope modulation and regular and irregular harmonic splitting. The mathematical and physical connections between the spectral modulation of high-order harmonics and the temporal modification of attosecond pulse train are explained. Based on these understandings, we propose a possible method to produce isolated attosecond pulses by tailoring surface the plasma profile.

DOI: [10.1103/PhysRevE.109.025212](https://doi.org/10.1103/PhysRevE.109.025212)**I. INTRODUCTION**

High-order harmonic generation (HHG) by the interaction of intense laser pulses with solid targets can provide a compact bright light source in the extreme ultraviolet and x-ray spectral range [1,2]. It has the potential to produce intense attosecond pulses [3–5]. Such sources can be achieved by three mechanisms depending on the laser intensity and plasma parameters: coherent wake emission (CWE) [6], relativistically oscillating mirror (ROM) [7–9], and coherent synchrotron emission (CSE) [10]. The emitted harmonics usually have a unique spectral shape. In the relativistic domain, harmonic spectrum is found to follow power-law or exponential scalings [10–15]. This makes the harmonic intensity I decline monotonically with the harmonic order n .

Some studies have found that the harmonic spectrum could deviate from the monotonic decline under some specific conditions. Early experimental results obtained with a picosecond laser showed a modulation of the harmonic spectrum envelope in the whole spectral range [16], so that some orders of the harmonics are enhanced. Watts *et al.* attributes such modulation to the higher modes of critical surface oscillation when the preplasma with a long scale length is compressed by a long laser pulse [16]. When harmonics are driven by laser pulses with shorter duration, Teubner *et al.* showed that the modulation of spectral envelope originates from the complex electron-density profile evolution due to the interplay of resonance absorption and ponderomotive force [17]. Using particle-in-cell (PIC) simulations, Boyd *et al.* revealed another mechanism for the harmonic spectral modulation, showing that the plasma waves excited in the overdense plasma could modulate the harmonic spectrum at the plasma frequency ω_p [18].

Modulated harmonic spectra could surpass the monotonic spectral decline if the surface plasma, so-called preplasma

in experiments, is steepened [16–18]. Recently, we experimentally demonstrated a scheme to actively steepen the preplasma with a normally incident circularly polarized prepulse [19]. We observed the modulated harmonic spectrum, which indicated a sharp truncation of preplasma. Meanwhile, each harmonic showed regular or irregular harmonic splitting in our experiment. However, the harmonic splitting is usually observed with large-scale-length preplasma [20–22], which is not the case for our experiment.

We found that the harmonic splitting should be attributed to the relativistic self-phase modulation (RSPM) of the drive laser when it passes through a residual underdense preplasma. The RSPM occurs before the HHG process but can lead to the spectral splitting of subsequently generated harmonics. A comprehensive theoretical study on these spectral modulations is helpful to design the HHG experiments or even diagnose the preplasma profile. In this paper, we show that the spectral modulations correspond to different distributions of preplasma in front of solid targets. We analyze the modulation mechanism and reveal the relation between spectral modulations and attosecond pulse train by using PIC simulations. Based on these understandings, a possible method to produce isolated attosecond pulse by tailoring surface plasma profile are discussed.

II. SPECTRAL MODULATION OF HIGH-ORDER HARMONICS

The spectral modulation of high-order harmonics is related to both the laser pulse characteristics and the preplasma profile. Basically, the laser pulse characteristics, such as the prepulse intensity and the laser chirp, will affect the HHG by modifying the preplasma profile before the pulse peak arrives at the target surface. To simplify the discussion, we fix the parameters of the drive laser and investigate the spectral modulation with different preplasma profiles.

*liuf001@sjtu.edu.cn

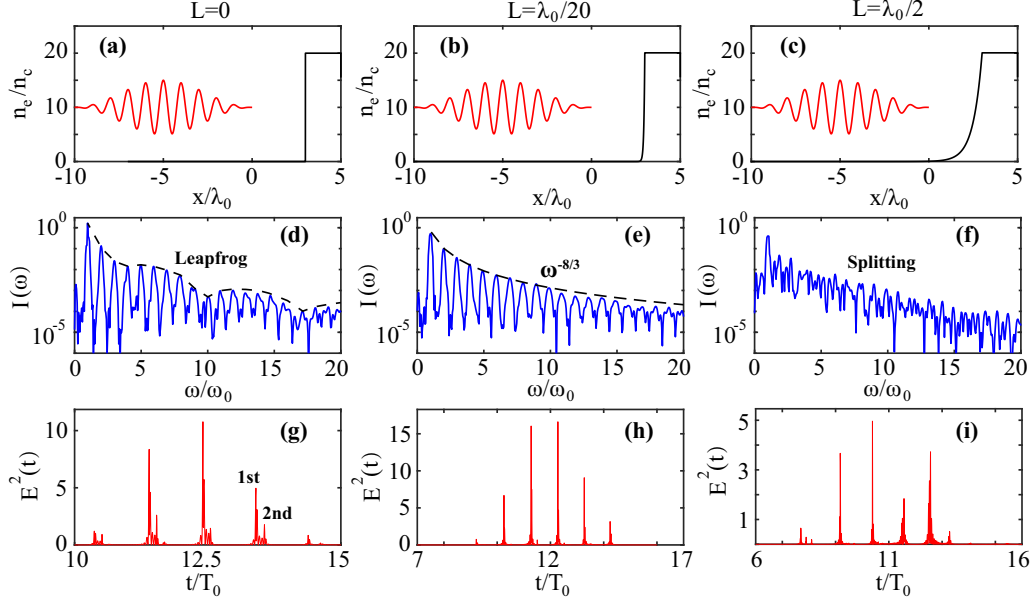


FIG. 1. Generation of high-order harmonics and attosecond pulses with different preplasma profiles. The left, middle, and right columns represent the target with a preplasma scale length of $L = 0$, $\lambda_0/20$, and $\lambda_0/2$, respectively. The upper row shows the drive laser and plasma density profiles. The middle row depicts the harmonic spectra, where $I(\omega)$ is normalized. The bottom row plots the attosecond pulse trains (filtered by $\omega/\omega_0 \geq 10$), where $E(t)$ is normalized by $E_0 = m_e \omega_0 c/e$.

As shown in Fig. 1, the laser pulse is p polarized and has a duration of $\tau = 10T_0$, where $T_0 = \lambda_0/c$ is the laser period and λ_0 is the laser wavelength. It has a pulse shape of $a = a_0 \sin^2(\pi t/\tau)$, where $a_0 = 5$ is the laser peak amplitude. We have performed both one-dimensional (1D) and two-dimensional (2D) PIC simulations. Results show that the spectral modulation of high-order harmonics is a quasi-1D issue. 1D and 2D simulation results have similar spectral shapes without considering the far-field propagation effect. Therefore, we mainly discuss the 1D situations in this paper. Grid size in the 1D simulations is $\lambda_0/1000$; 100 electrons and ions are put into each grid. To observe the HHG with oblique incidence, transversely moving frame used by Lichters *et al.* [23] is introduced in our simulations. All the particles have an initial transverse momentum of $\gamma v_{\perp}/c = -1$, which represents that the laser incident angle is 45° . The target has a bulk plasma density of $n_0 = 20n_c$, where n_c is the critical plasma density of the laser. The preplasma density rises exponentially as $n_e = n_0 e^{(x-3\lambda_0)/L}$ when $x < 3\lambda_0$, where L is the scale length.

We select three typical cases that can produce representative spectral shapes here. First, we assume a step-like plasma density profile with $L = 0$, as shown in Fig. 1(a). The generated harmonic spectrum is obtained by the Fourier transform of reflected laser, which is depicted in Fig. 1(d). It can be seen that the harmonic intensity does not decline monotonically with harmonic order. The spectral envelope presents a *leapfrog* feature with a period of $\Delta\omega = 6-7\omega_0$, which is larger than the plasma frequency $\omega_p \approx 4.5\omega_0$ corresponding to the plasma density. Among each leapfrog, the harmonic spectrum becomes flatter. Then, we introduce some preplasma in front of the target with a scale length of $L = \lambda_0/20$ [Fig. 1(b)]. Now as depicted in Fig. 1(e), the harmonic spectrum becomes

monotonically declining, following the power-law scaling of $I(\omega) \propto \omega^{-8/3}$ predicted by ROM [11]. We further increase the preplasma scale length to $L = \lambda_0/2$ [Fig. 1(c)]. The spectrum in Fig. 1(f) indicates that each harmonic is strongly split in this case.

To better understand the underlying physics for the harmonic spectral modulations arising from the three different preplasma profiles, we investigate the emitted attosecond pulse train in the temporal domain. The maximum plasma density of $20n_c$ implies that CWE is excluded for all harmonics with $n > 4.5$. All temporal pulse trains are obtained by selecting harmonics with $n \geq 10$. As shown in Fig. 1(h), the attosecond pulse train has a Gaussian-like envelope and the time intervals between successive attosecond pulses are constant for $L = \lambda_0/20$. For $L = 0$ with a leapfrog spectrum, harmonics are radiated twice in each laser cycle while the attosecond pulse train still has a Gaussian-like envelope [Fig. 1(g)]. However, for $L = \lambda_0/2$ when the harmonic spectrum strongly split, the envelope of attosecond pulse train is remarkably modified and the temporal intervals between two successive attosecond pulses also change [Fig. 1(i)]. The above results have shown HHG by ROM with three typical preplasma profiles. In the next section, we discuss the connection between the temporal modification of attosecond pulse train and the spectral modulation of high-order harmonics in detail.

III. HARMONIC SPECTRUM MODULATION MECHANISM

The attosecond pulse train can be expressed as $E(t) = \sum_m E_m f(t - t_m)$, where E_m and $f(t)$ are the amplitude and temporal shape function of the m th attosecond pulse. Normally, one attosecond pulse is emitted in each laser cycle

with equal temporal spacing ($t_m = 2\pi m/\omega_0$), so the Fourier transform of $E(t)$ is

$$\tilde{E}(\omega) = F(\omega) \sum_{m=1}^M E_m e^{-j(2\pi m\omega)/\omega_0}, \quad (1)$$

where M is the total number of attosecond pulses. Equation (1) gives a regular harmonic spectrum, which usually has no spectral modulation. However, as shown in Figs. 1(g) and 1(i), attosecond pulses could also be emitted twice in one laser cycle and the temporal spacing may be unequal. Then, the shape function $f(t)$ becomes $f(t) + \alpha_m f(t - \Delta t)$ and the emission time t_m becomes $t_m = 2\pi(m + d_m)/\omega_0$, where α_m represents the relative field strength of the secondary emission, $\Delta t = 2\pi\beta/\omega_0$ ($|\beta| < 1/2$ for $|\Delta t| < T_0/2$) is the delay between two emissions within one laser cycle, and d_m is the relative time shift in each laser period. With these variations in temporal domain, the Fourier transform of $E(t)$ in the frequency domain is modified as

$$\tilde{E}(\omega) = F(\omega) \sum_{m=1}^M (1 + \alpha_m e^{-j(2\pi\beta\omega)/\omega_0}) E_m e^{-j[2\pi(m+d_m)\omega]/\omega_0} \quad (2)$$

The coherent superposition term $e^{-j(2\pi m\omega)/\omega_0}$ in Eq. 2 makes the spectrum peak at integers $\omega/\omega_0 = n$ to produce harmonics. Other than this term, there are three additional terms related to m ($\alpha_m e^{-j(2\pi\beta\omega)/\omega_0}$, E_m , and $e^{-j(2\pi d_m\omega)/\omega_0}$) which lead to the modulation of high-order harmonic spectrum.

First, the term $\alpha_m e^{-j(2\pi\beta\omega)/\omega_0}$ brings the envelope modulation. Harmonic intensity could be enhanced if $\omega = \frac{p}{\beta}\omega_0$, where $p = 0, 1, 2, \dots$. This makes the harmonic spectrum peak at the order p/β with a leapfrog step $\Delta\omega/\omega_0 = 1/\beta$. Second, the term E_m brings regular splits of the harmonic spectrum. Referring to Fig. 1(i), we assume that E_m has a low-frequency fluctuation of $E_m = \sin(2\pi m/4) = j(e^{-j(2\pi m)/4} - e^{j(2\pi m)/4})/2$. Combining with the term $e^{-j(2\pi m\omega)/\omega_0}$, it can be found that the initial harmonic peak at an integer order $\omega/\omega_0 = n$ will be split into two peaks at the noninteger orders $\omega/\omega_0 = n \pm 1/4$. Third, the term $e^{-j(2\pi d_m\omega)/\omega_0}$ brings irregular splits of the harmonic spectrum. If d_m changes proportionally with m , which means the temporal intervals between two successive attosecond pulses are different from T_0 but keep constant, the harmonic spectrum would not get split but have an overall frequency shift. However, mostly d_m does not change proportionally with m . This makes the frequency shift irregular and finally results in chaotic splits of the harmonic spectrum.

These three kinds of spectral modulations can be checked by numerical calculations. We separately extract the temporal envelope of E_m and the time shift d_m from Figs. 1(g)–1(i), which are shown in Figs. 2(a) and 2(b). One can see the Gaussian-like temporal envelope for $L = 0$ and $\lambda_0/20$ but a sine-like envelope for $L = \lambda_0/2$. The time shift is nearly zero for $L = 0$ and $\lambda_0/20$ but changes significantly for $L = \lambda_0/2$. We begin with an attosecond pulse train with six Gaussian pulses. Each pulse has the same amplitude and duration of $0.1\pi/\omega_0$. Figure 2(c) shows the harmonic spectrum when the train is modified by the temporal envelope and time shift of $L = \lambda_0/20$. No spectral modulation can be seen on this spectrum. It is similar when the temporal envelope and time shift

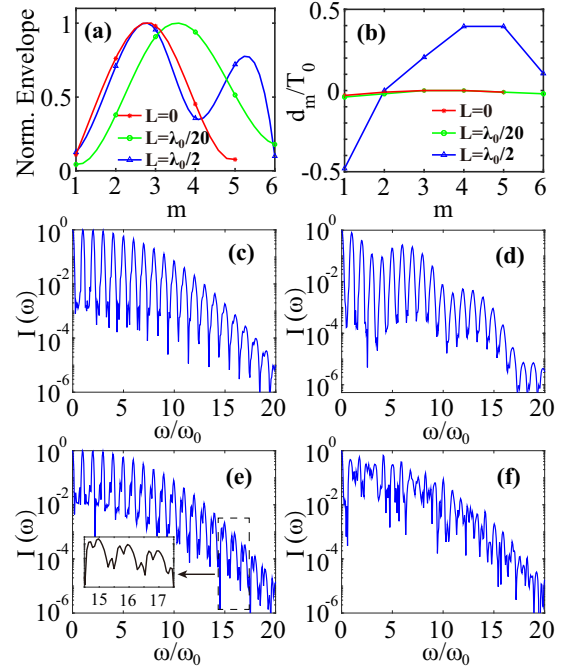


FIG. 2. (a) Normalized temporal envelopes and (b) emission time shifts of the three attosecond pulse trains in Fig. 1. The lines in panel (a) show the spline fitting of the data. Panels (c)–(f) show the normalized harmonic spectra when a train of uniform attosecond pulses is modulated with different envelopes and times shifts: (c) both envelope and time shift from $L = \lambda_0/20$, (d) both envelope and time shift from $L = 0$ but two attosecond pulses in a laser cycle with a delay of $1/\omega_0$, (e) only envelope from $L = \lambda_0/2$ without time shift, and (f) only time shift from $L = \lambda_0/2$ without envelope change.

of $L = 0$ are applied to the attosecond pulse train. However, for $L = 0$ there should be two pulses in each laser cycle. According to Fig. 1(g), we add a secondary pulse in each laser cycle. The secondary pulse is at a delay of $\Delta t = 1/\omega_0$ and has a relative field strength of $1/4$ with respect to the initial pulse. Now, the broad spectral envelope modulation with a leapfrog step $\Delta\omega = 2\pi$ can be clearly observed on the harmonic spectrum. For $L = \lambda_0/2$, both the temporal envelope and the time shift of the attosecond pulse train are significantly modified, so we discuss the two effects separately. Figure 2(e) shows the harmonic spectrum when only the temporal envelope modification shown in Fig. 2(a) is considered. It can be seen that each harmonic is regularly split into two peaks. Such regular splitting has been experimentally observed [19,24]. Figure 2(f) shows the harmonic spectrum when only the time shift is considered. In this case, the harmonic splitting becomes irregular.

In the above, we have mathematically explained that the spectral modulation can be attributed to three kinds of temporal modifications of attosecond pulse trains. All of them have physically corresponding factors. The temporal modification of attosecond pulse trains originates from the relativistic oscillation of surface plasma affected by the plasma profile or drive laser. For the ideal situation, a laser pulse should be reflected at the surface of the critical plasma density. Electrons will be driven to resonantly oscillate with the laser and radiate

once in a laser cycle. However, the plasma density at the solid targets surface is highly overcritical if no preplasma exists. Surface electrons will oscillate with a frequency higher than the laser frequency and consequently two or more attosecond pulses will be emitted in a laser cycle [25]. In contrast, if the preplasma has a large scale length, the reflection surface will move during the interaction due to the laser ponderomotive force. Therefore, the temporal spacing of attosecond pulses are constantly changed. The ponderomotive effect has been explained in detail in Ref. [20]. The dynamics of surface plasma alone cannot completely explain the temporal modification of attosecond pulses, such as the envelope of E_m . We note that the RSPM [26] of laser pulse also plays an important role in the temporal modification of attosecond pulses and spectral modulation of high-order harmonics.

We give an estimate of the RSPM with a simplified model. The phase shift of a relativistic laser in plasma is [26]

$$\phi = \frac{\omega_0}{c} \int_0^{x_{\text{cut}}} \left[1 - \frac{n_e(x)}{\gamma n_c} \right]^{1/2} dx, \quad (3)$$

where $\gamma = (1 + a^2/2)^{1/2}$ is the Lorentz factor. To be simple, we assume that the plasma has a linear density profile $n_e(x) = n_c x/x_c$. The phase shift can be calculated as

$$\phi = \frac{4\pi\gamma x_c}{3\lambda_0} \left[1 - \left(1 - \frac{x_{\text{cut}}}{\gamma x_c} \right)^{3/2} \right]. \quad (4)$$

When analyzing a spectrum, the absolute phase shift is not the most important. More critical parameter is the relative phase shift among laser cycles. We define the phase at the peak cycle as the zero-phase point. Then the relative phase shift becomes $\Delta\phi = \phi(\gamma_{\text{max}}) - \phi(\gamma)$. Now, two situations can be discussed. Normally, the preplasma rises continuously from $n_e = 0$ to the solid density. Considering the relativistic self-transparency [27], the laser will be reflected almost at $x_{\text{cut}} = \gamma x_c$. The relative phase shift becomes

$$\Delta\phi = \frac{4\pi x_c}{3\lambda_0} (\gamma_{\text{max}} - \gamma). \quad (5)$$

In another special situation, the preplasma may be truncated, like the modified preplasma profile in Ref. [19]. Assuming preplasma being truncated at $x_{\text{cut}} = \eta x_c$ ($\eta \ll \gamma$), the relative phase shift becomes

$$\Delta\phi \sim \eta^2 \frac{\pi x_c}{2\lambda_0} \left(\frac{1}{\gamma} - \frac{1}{\gamma_{\text{max}}} \right), \quad (6)$$

with the second-order Taylor expansion of Eq. (4). From Eqs. (5) and (6), it can be found that $\Delta\phi$ is larger for a longer preplasma scale length and a laser cycle farther away from the peak. Furthermore, the rising edge of laser pulse will be compressed and the falling edge of laser pulse will be elongated. Note that the analyses here can only qualitatively estimate the relative phase shift. The real process of RSPM, which includes the dynamics of plasma oscillation driven by the laser fields and its reaction to the relativistic laser pulse, is more complex. Therefore, the amplitude modulation of laser pulse is hard to analytically calculate. We investigate the dynamic process of RSPM by PIC simulations.

In the simulation, we artificially separate a truncated preplasma from the target with a vacuum gap between them.

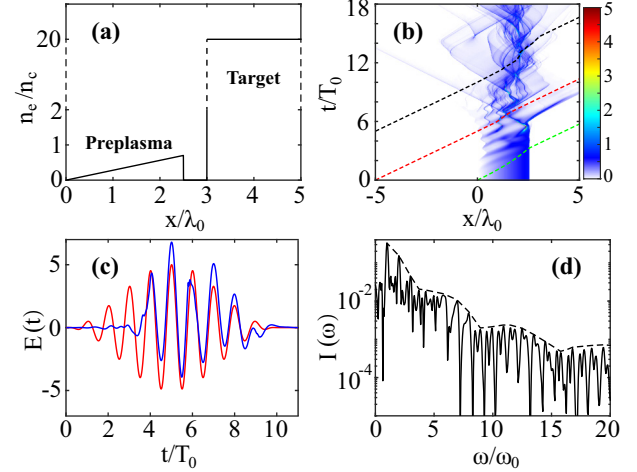


FIG. 3. Illustration of the effect of RSPM on HHG. (a) Plasma density profile. (b) Evolution of the preplasma density and the front-to-end position of laser pulse when removing the target. The green, red, and black dashed lines represent the positions of pulse front, peak, and end, respectively. (c) Laser waveform after passing through the preplasma in panel (a), where the red and blue lines are the laser pulses before and after propagation through the preplasma, respectively. (d) Harmonic spectrum obtained for the plasma profile shown in panel (a).

Such profile refers to the experimentally modified preplasma in Ref. [19]. As shown in Fig. 3(a), the preplasma density linearly rises from 0 to a maximum of $0.7n_c$; the gap between the preplasma and target is $0.5\lambda_0$. With such plasma density setting, the modification of the laser pulse in the preplasma could be decoupled from the HHG in the overdense plasma, and the moving of plasma surface is avoided as well. We first investigate the laser modulation in the preplasma. Figure 3(b) shows the evolution of the preplasma density and the front-to-end position of the laser pulse without the target. The compression of pulse rising edge and the elongation of pulse falling edge can be clearly observed after the laser passes through the preplasma. During the process, strong oscillation of the preplasma is excited by the laser fields. For some cycles, the laser will experience a plasma barrier with relatively high density, which reduces the laser transmission ratio. Figure 3(c) shows the laser waveform after passing through the preplasma. One can find the amplitude modulation and the relative phase shift. Owing to the compression of pulse rising edge, the peak intensity of laser pulse even exceeds the initial value. Besides, because we assume the transverse moving frame moves in the positive direction in our simulation, electrons tend to be pushed forward in the positive half cycles of the laser pulse, which causes the negative cycles to experience a higher plasma barrier and lower transmission ratio. When such modulated laser impinges on the target, attosecond pulses will be emitted with temporal modifications both on the amplitude envelope and the time spacing. Thus, both the regular and chaotic harmonic splitting can be found in the reflected laser spectrum, as shown in Fig. 3(d). Meanwhile, because the target density is far larger than n_c , the leapfrog spectral modulation can also be observed.

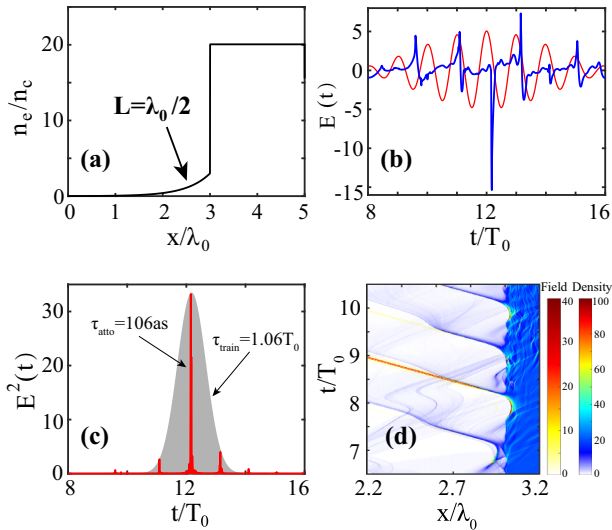


FIG. 4. (a) Tailored plasma density profile for isolated attosecond pulse generation. (b) Incident (red line) and reflected (blue line) laser waveforms. (c) Attosecond pulses after filtering the reflected laser with $\omega/\omega_0 \geq 10$. (d) Spatiotemporal evolution of plasma density and attosecond pulse emission.

IV. ISOLATED ATTOSECOND PULSE

Based on the above understanding of harmonic spectral modulation mechanism, specially designed surface plasma profiles can be used to control the high-order harmonic emission for applications. An important application of high-order harmonics is to probe attosecond physical process by acquiring an isolated attosecond pulse [28]. To get an isolated attosecond pulse, many methods have been proposed, such as using few-cycle laser [29], attosecond lighthouse [30], and polarization gating [31]. All of these methods rely on the manipulation of laser spatiotemporal properties. Here, we propose a possible method to produce isolated attosecond pulse by tailoring the surface plasma profile.

Mathematically, a flat and continuous spectrum is beneficial for the generation of an isolated attosecond pulse. This inspires us that combining the spectra of Figs. 1(d) and 1(f) may produce an isolated attosecond pulse. To examine the feasibility, we design a tailored plasma profile where a long-scale preplasma is followed by a step-like target. As shown in Fig. 4(a), the plasma profile is set to be a preplasma of $L = \lambda_0/2$ followed by an overdense target of $L = 0$. The maximum density of preplasma is $n_e = 3n_c$ and the density of overdense target is $n_e = 20n_c$. Such a profile may be implemented in experiments by coating thin near-critical-density CH or carbon-nanotube foams on the surface of solid targets [32]. It should be noted that the plasma density is not limited to the parameters here. n_e can be scaled with the laser amplitude a_0 while fixing the similarity parameter $S = n_e/a_0n_c$. The preplasma scale length can be precisely controlled by a prepulse as done in Ref. [33].

Figure 4(b) shows the comparison between incident and reflected laser waveforms. It can be seen that a very sharp peak with high-frequency components is generated only in the laser peak cycle. We also extract the harmonics of $\omega/\omega_0 \geq 10$. Figure 4(c) shows the generated attosecond pulse train. The

TABLE I. Generation efficiency of attosecond pulses with different plasma profiles.

Profiles	$L = 0$	$L = \lambda_0/20$	$L = \lambda_0/2$	Tailored
Efficiency	2.08%	2.55%	1.13%	2.02%

radiation intensities in the side cycles are below $1/e^2$ of those in the laser peak cycle. An isolated attosecond pulse with a duration of 106 as (FWHM) is achieved. We find that the generation efficiency in the isolated attosecond pulse is close to the $L = 0$ case. Table I shows the attosecond pulse generation efficiency $\int E_{\text{atto}}^2(t)dt / \int E_{\text{laser}}^2(t)dt$ with different plasma profiles. For the case with tailored plasma profile, only the intensity of isolated attosecond pulse is integrated. It can be found that the HHG efficiency of isolated attosecond pulse in the tailored case almost equals to the overall efficiency of the whole attosecond pulse train in the $L = 0$ case. This efficiency is much higher than the nontailored $L = \lambda_0/2$ case.

To explore the specific physics for isolated attosecond pulse generation, the spatiotemporal evolution of plasma density and the corresponding attosecond radiation are diagnosed, as shown in Fig. 4(d). Because the existence of long-scale preplasma, high-order harmonics cannot be radiated efficiently at the laser rising edge. However, different from the case of $L = \lambda_0/2$, electrons at the surface of step-like target are piled up by the ponderomotive force of laser rising edge for the case with tailored plasma profile. As a result, the laser peak cycle will interact with an ultrathin and high-density electron layer. An intense attosecond pulse is emitted by the CSE mechanism [10] during the interaction. And the secondary emission from the step-like target is suppressed in the laser peak cycle. Due to the background ions are immobile in such short time, the electrostatic force will make the ultrathin electron layer collapse rapidly when the ponderomotive force falls. Thus, high-order harmonics are also radiated inefficiently at the laser falling edge.

We have also investigated the robustness of isolated attosecond pulse generation by tailoring the surface plasma profile. As shown in Fig. 4(b), the isolated attosecond pulse is generated when the electric field of the reflected laser is negative. Therefore, the carrier envelope phase (CEP) may be an important factor. We refer to the characterization method in Ref. [29]. Gaussian fitting $E_{\text{train}}^2(t) \propto \exp(-4 \ln 2 t^2 / \tau_{\text{train}}^2)$ is performed to characterize the attosecond pulse train envelope, where τ_{train} represents the FWHM duration of the pulse train. Figure 5(a) shows the variation of τ_{train} with the CEP of laser pulse. We find that when $\tau_{\text{train}} > 1.45$ (dashed line), there will be two attosecond pulses in τ_{train} . For CEP $\in [-\pi/3, 2\pi/3]$, an isolated attosecond pulse can be obtained. The laser pulse shape and duration can also affect the generation of isolated attosecond pulse. As illustrated in Fig. 4(d), the ponderomotive force of the laser rising edge is crucial. Therefore, the duration of laser rising edge should be short to produce the ultrathin surface electron layer. However, the laser falling edge could be long. Figure 5(b) shows the attosecond pulse train obtained by a laser pulse with $5T_0$ rising edge and $10T_0$ falling edge. The feature of the isolated attosecond pulse still keeps.

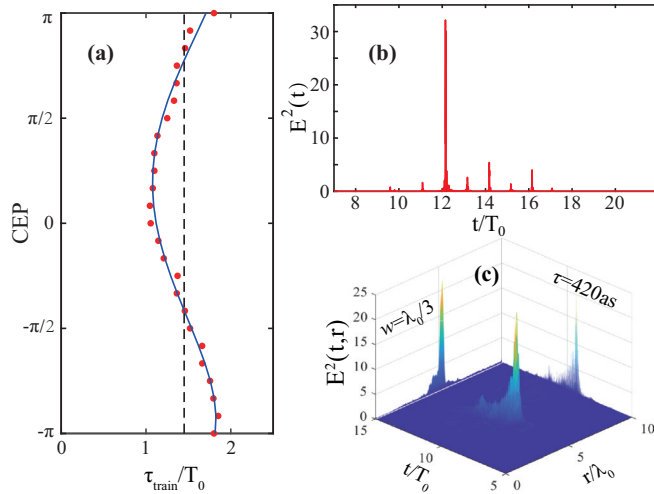


FIG. 5. (a) Variation of the pulse train width τ_{train} (FWHM) with the CEP of laser pulse. The solid line is a quadratic fitting of the data. There will be two attosecond pulses within τ_{train} if the data exceed the dashed line. (b) Attosecond pulse train for a laser pulse with $5T_0$ rising edge and $10T_0$ falling edge. (c) Feature of isolated attosecond pulse in a 2D simulation.

Finally, we also performed a 2D simulation to verify this scheme. The grid size in the 2D simulation is $\Delta x = \Delta y = \lambda_0/100$ and 49 electrons are put in each grid. The laser transverse shape is set to $a = a(t) \exp(-r^2/w_0^2)$, where $w_0 = 3\lambda_0$ is the beam waist. Other parameters are the same as what was set in 1D simulations. Figure 5(c) shows the 2D simulation result. An isolated attosecond pulse can still be observed with a pulse width (FWHM) of $\tau = 420$ as. Besides, the attosecond pulse is further found to be spatially gated because the ultrathin electron layer cannot be formed at the edge of laser

beam. The simulation result shows that the attosecond pulse of $n > 10$ harmonics only has a source size of $w = \lambda_0/3$, one order of magnitude smaller than the spot size of the drive laser.

V. SUMMARY

In summary, we have investigated the spectral modulation of high-order harmonics generated in relativistic laser-solid interactions. Based upon numerical simulations and theoretical analyses, three kinds of harmonic spectral modulations: envelope modulation, regular harmonic splitting, and irregular harmonic splitting, are discussed. These are associated with the temporal structure of attosecond pulse radiation. The harmonic spectral modulation physically originates from the higher modes of surface plasma oscillation, temporal moving of the reflection surface, and relativistic self-phase modulation. This work gives a detailed understanding of the spectral and temporal features of high-order harmonic emission by relativistic lasers. Based on these understandings, we further give a possible method to produce isolated attosecond pulse by tailoring surface plasma profile. Besides, spectral modulation of high-order harmonics may be a tool to diagnose the surface plasma profile of solid targets.

ACKNOWLEDGMENTS

The authors would like to thank the Supercomputer Center at SJTU for providing computing resources. This work was supported by Shanghai Jiao Tong University 2030 Initiative (WH510363002/007), the National Natural Science Foundation of China (Grants No. 11991074, No. 12175140, No. 11905129, and No. 12135009), and the strategic Priority Research Program of the Chinese Academy of Sciences (Grants No. XDA25010500, No. XDA25010100, and No. XDA25050000).

- [1] U. Teubner and P. Gibbon, *Rev. Mod. Phys.* **81**, 445 (2009).
- [2] S. Haessler *et al.*, *Ultrafast Sci.* **2022**, 9893418 (2022).
- [3] C. Thauray and F. Quéré, *J. Phys. B: At., Mol. Opt. Phys.* **43**, 213001 (2010).
- [4] L. Chopineau, A. Denoëud, A. Leblanc, E. Porat, P. Martin, H. Vincenti, and F. Quéré, *Nat. Phys.* **17**, 968 (2021).
- [5] H. Vincenti, *Phys. Rev. Lett.* **123**, 105001 (2019).
- [6] F. Quéré, C. Thauray, P. Monot, S. Dobosz, Ph. Martin, J.-P. Geindre, and P. Audebert, *Phys. Rev. Lett.* **96**, 125004 (2006).
- [7] S. V. Bulanov, N. M. Naumova, and F. Pegoraro, *Phys. Plasmas* **1**, 745 (1994).
- [8] D. von der Linde, T. Engers, G. Jenke, P. Agostini, G. Grillon, E. Nibbering, A. Mysyrowicz, and A. Antonetti, *Phys. Rev. A* **52**, R25(R) (1995).
- [9] P. Gibbon, *Phys. Rev. Lett.* **76**, 50 (1996).
- [10] D. an der Brügge and A. Pukhov, *Phys. Plasmas* **17**, 033110 (2010).
- [11] T. Baeva, S. Gordienko, and A. Pukhov, *Phys. Rev. E* **74**, 046404 (2006).
- [12] T. G. Blackburn, A. A. Gonoskov, and M. Marklund, *Phys. Rev. A* **98**, 023421 (2018).
- [13] M. R. Edwards, N. M. Fasano, and J. M. Mikhailova, *Phys. Rev. Lett.* **124**, 185004 (2020).
- [14] M. R. Edwards and J. M. Mikhailova, *Sci. Rep.* **10**, 5154 (2020).
- [15] S. Bhadoria, T. Blackburn, A. Gonoskov, and M. Marklund, *Phys. Plasmas* **29**, 093109 (2022).
- [16] I. Watts, M. Zepf, E. L. Clark, M. Tatarakis, K. Krushelnick, A. E. Dangor, R. M. Allott, R. J. Clarke, D. Neely, and P. A. Norreys, *Phys. Rev. Lett.* **88**, 155001 (2002).
- [17] U. Teubner, G. Pretzler, Th. Schlegel, K. Eidmann, E. Förster, and K. Witte, *Phys. Rev. A* **67**, 013816 (2003).
- [18] T. J. M. Boyd and R. Ondarza-Rovira, *Phys. Rev. Lett.* **98**, 105001 (2007).
- [19] B. Y. Li, F. Liu, M. Chen, F. Y. Wu, J. W. Wang, L. Lu, J. L. Li, X. L. Ge, X. H. Yuan, W. C. Yan, L. M. Chen, Z. M. Sheng, and J. Zhang, *Phys. Rev. Lett.* **128**, 244801 (2022).
- [20] M. Behmke, D. an der Brügge, C. Rödel, M. Cerchez, D. Hemmers, M. Heyer, O. Jäckel, M. Kübel, G. G. Paulus, G. Pretzler, A. Pukhov, M. Toncian, T. Toncian, and O. Willi, *Phys. Rev. Lett.* **106**, 185002 (2011).
- [21] C. Rödel, D. an der Brügge, J. Bierbach, M. Yeung, T. Hahn, B. Dromey, S. Herzer, S. Fuchs, A. Galesian Pour, E. Eckner, M. Behmke, M. Cerchez, O. Jäckel, D. Hemmers, T. Toncian,

- M. C. Kaluza, A. Belyanin, G. Pretzler, O. Willi, A. Pukhov, M. Zepf, and G. G. Paulus, *Phys. Rev. Lett.* **109**, 125002 (2012).
- [22] F. Dollar, P. Cummings, V. Chvykov, L. Willingale, M. Vargas, V. Yanovsky, C. Zulick, A. Maksimchuk, A. G. R. Thomas, and K. Krushelnick, *Phys. Rev. Lett.* **110**, 175002 (2013).
- [23] R. Lichters, J. Meyer-ter-Vehn, and A. Pukhov, *Phys. Plasmas* **3**, 3425 (1996).
- [24] J. Braenzel, A. Andreev, M. Schnürer, S. Steinke, K. Platonov, G. Priebe, and W. Sandner, *Phys. Plasmas* **20**, 083109 (2013).
- [25] B. Y. Li, F. Liu, M. Chen, Z. Y. Chen, X. H. Yuan, S. M. Weng, T. Jin, S. G. Rykovanov, J. W. Wang, Z. M. Sheng, and J. Zhang, *Phys. Rev. E* **100**, 053207 (2019).
- [26] I. Watts, M. Zepf, E. L. Clark, M. Tatarakis, K. Krushelnick, A. E. Dangor, R. Allott, R. J. Clarke, D. Neely, and P. A. Norreys, *Phys. Rev. E* **66**, 036409 (2002).
- [27] V. I. Eremin, A. V. Korzhimanov, and A. V. Kim, *Phys. Plasmas* **17**, 043102 (2010).
- [28] F. Krausz and M. Ivanov, *Rev. Mod. Phys.* **81**, 163 (2009).
- [29] P. Heissler, R. Hörlein, J. M. Mikhailova, L. Waldecker, P. Tzallas, A. Buck, K. Schmid, C. M. S. Sears, F. Krausz, L. Veisz, M. Zepf, and G. D. Tsakiris, *Phys. Rev. Lett.* **108**, 235003 (2012).
- [30] H. Vincenti and F. Quéré, *Phys. Rev. Lett.* **108**, 113904 (2012).
- [31] M. Yeung, J. Bierbach, E. Eckner, S. Rykovanov, S. Kuschel, A. Sävert, M. Förster, C. Rödel, G.G. Paulus, S. Cousens, M. Coughlan, B. Dromey, and M. Zepf, *Phys. Rev. Lett.* **115**, 193903 (2015).
- [32] W. J. Ma, I. Jong Kim, J. Q. Yu, Il, W. Choi, P. K. Singh, H. W. Lee, J. H. Sung, S. K. Lee, C. Lin, Q. Liao, J. G. Zhu, H. Y. Lu, B. Liu, H. Y. Wang, R. F. Xu, X. T. He, J. E. Chen, M. Zepf, J. Schreiber, X. Q. Yan, and C. H. Nam, *Phys. Rev. Lett.* **122**, 014803 (2019).
- [33] S. Kahaly, S. Monchocé, H. Vincenti, T. Dzelzainis, B. Dromey, M. Zepf, Ph. Martin, and F. Quéré, *Phys. Rev. Lett.* **110**, 175001 (2013).